Reliable $Pb(Zr,Ti)O_3$-based thin film piezoelectric micromirrors for space-applications

Runar Dahl-Hansen[1], Jo Gjessing[1], Peter Mardilovich[2], Charalampos Fragkiadakis[2], and Jostein Thorstensen[1]
[1]SINTEF, Forskningsveien 1, 0373, Oslo, Norway
[2]AixACCT Systems GmbH, Talbotstr. 25, 52068 Aachen, Germany

(Mail: runard@sintef.no)

Abstract

Although $Pb(Zr,Ti)O_3$ (PZT) piezoelectric thin films are finding widespread applications on Earth, it is yet unclear if they are suitable for space-related applications. In space, their long-term reliability is a significant concern due to the difficulties of repairing and replacing malfunctioning devices. In this work, PZT thin film micromirrors for compact interferometric 3D imaging systems have been exposed to operating conditions encountered on a space mission and tested according to criteria set by the European Space Agency. Thermal cycling in vacuum, sinusoidal and random mechanical vibrations, and γ-radiation with and without bias did not degrade key functional device properties of the micromirror; angular deflection, resonance frequency, polarization, and permittivity. Apart from γ-radiation, stressing the devices enhanced their large-signal angular deflection and improved their electrical lifetime compared to pristine devices. Their dielectric and ferroelectric characteristics remained comparable to that of a lab-scale environment. Simultaneously applying a 10 V field-down bias while γ-radiating the micromirrors changed the capacitance-field and polarization-field characteristics and enhanced the electrical imprint. After stress-testing, the median time-to-failure in moderate acceleration conditions of 150 kV/cm and 175°C, ranged from 1.95 to 2.64 h, close to 2.11 h as measured for a reference group. All actuator membranes had shorter electrical lifetimes, smaller voltage acceleration factors, and smaller activation energies, ranging from 2.56 to 2.88 V^{-1} and 1.03 to 1.09 eV, than simple bonding pads. This work is a device-level report covering a full set of space-relevant tests demonstrating that PZT-based thin film piezoMEMS technology is space-ready.

3D imaging technology is essential for aiding autonomy and robotics on space missions, during e.g., docking, sample collection, and navigation[1]. Reducing the overall space mission complexity thereby requires compact 3D-imaging systems with low power consumption, low weight, high robustness, and sub-mm accuracy[2]. These requirements can be satisfied using a Michelson interferometry-based approach, whereby 3D images are reconstructed from interferometric fringe patterns projected onto the object to be imaged[1,3]. Full 3D image reconstruction necessitates tiltable micromirrors capable of deflecting in the nm to µm range with nm-scale accuracy, nm-scale position-repeatability, and sub-millisecond repositioning times. To avoid complications with malfunctioning or failing components, the reliability is a key concern, in particular for the sensitive micromirror of the interferometer.

Sensors and actuators for space missions should generally possess properties typically inherent in microelectromechanical systems (MEMS), such as small size, low power consumption, and high robustness[4]. Micromirrors satisfying these criteria can be realized using thin film piezoelectric MEMS (piezoMEMS) as they offer large mechanical deflections at low voltages, scalability, low power consumption, and high temperature-stability over a large range of frequencies[5–8]. Due to its high piezoelectric response and large blocking pressure, $Pb(Zr,Ti)O_3$ (PZT) is currently the material of choice for a wide range of thin film piezoMEMS, including micro-robotics[9], energy-harvesting[10], ultrasound transduction[11–13], and microoptics[8,14,15]. In previous work, the Michelson 3D imaging system described above was realized using a PZT-based thin film piezoelectric micromirror[1]. This work assesses the reliability of such thin film piezoMEMS micromirrors, covering a complete set of space-relevant test conditions.

This is the authors accepted manuscript of an article published in
Applied Physics Letters 2022, 121, 132901.
http://dx.doi.org/10.1063/5.0106933

The finalized piezoelectric layer-stack comprised of a 2 µm thick undoped $Pb(Zr_{0.52}Ti_{0.48})O_3$ (PZT, hereafter), deposited by chemical solution on $LaNiO_3$-coated platinized Si wafers. As the top electrode, 250 nm Au with a 10 nm Ti/10 wt% W adhesion layer was sputtered and structured before applying a 40 nm thick atomic layer-deposited Al_2O_3 barrier-layer. Figure 1 (a) and (b) show a to-scale schematic illustration of the device and layer-stack, indicating the applied electric field-down, i.e., Au as positive and $LaNiO_3$/Pt as negative electrodes across the stack for actuation.

On the finalized device, the 8 µm thick membrane with the actuators shaped as two concentric rings was reactive ion etched from the backside, defining the 400 µm thick center mirror. The rings are divided into four inner (I), and four outer (O) individually controllable sections with electrode areas of 1.07 and 1.21 mm^2, respectively. 20 µm wide Au lines routs each section to wire-bonding pads along the periphery of the 8x8 mm^2 die. Each micromirror also contains four unrouted simple 200x200 µm^2 square pads (capacitors) with an electrode area of 0.04 mm^2, also used for lifetime measurements. All routings and pads are clamped to the 400 µm thick Si chip handle. Further details and the micromirror's working principle can be found in previous reports[1,14,16,17]. This work assesses the functional properties and lifetime of the I/O actuator electrodes as well as the simple square wire-bonding pads. The devices were not poled before stress testing.

In collaboration with the European Space Agency (ESA), the ambient conditions experienced by the device during the launch, in-orbit, and on-destination operation phases on a typical space mission, were emulated for stress-testing. Figure 1 (c)-(e) shows the micromirrors mounted for the assigned stress tests; (A) TVAC, (B) random and sine X/Y/Z-vibrations, and (C) γ-radiation with and without an applied bias of 10 V, field-down. Figure 1 (f) summarizes the test parameters used for five test groups of micromirrors, including a cumulative, (D), and a reference, (E), group. To ensure similar electrical history, the test order remained the same throughout; initial characterization – stress test – post-test characterization – destructive, highly accelerated lifetime tests (HALT). Four micromirrors were put through each stress test, and each micromirror had 12 structured top electrodes. 16 I/O membrane actuators were stress-tested and characterized for each functional property. For the time-dependent dielectric breakdown (TDDB), all 16 I/O and 8 pads from each group were used. In addition, 5 separate reference sets from a different wafer of the same wafer batch were used to assess activation energies and acceleration factors, as shown in the supplementary information (SI).

Four sets of characterizations were performed before and after every stress test. These were (i) large-signal angular deflection (d_{LS}) at 100 kV/cm, (ii) frequency-sweeps at 5 kV/cm in the range of 0-10 kHz in steps of 100 Hz, (iii) bipolar and unipolar polarization vs. electrical field (P-E) at 100 Hz with a maximum amplitude of 100 kV/cm, and (iv) bipolar capacitance and loss vs. electrical field (C-E) with a small-signal amplitude of 200 mV, maximum field of 100 kV/cm and a small-signal frequency of 1 kHz. Pristine and stress-tested devices were compared using curves and a set of selected characteristics; d_{LS}, the mechanical mirror resonance, f_{res}, the positive-negative remnant polarization-difference, $2P_R$, the positive coercive field, E_C^+, imprint, $E_{C,shift} = \frac{E_C^+ - |E_C^-|}{2}$, the average permittivity over a full C-E loop, ϵ_{avg}, and the loss tangent, $\tan(\delta)$.

Electrical lifetimes were assessed by TDDB on both pristine and stress-tested samples at temperatures of 150-200 ^oC and electrical fields of 100 < E < 250 kV/cm. Weibull analysis was used to estimate the time-to-failure using the approach described in [18,19]:

$$P_f(t) = 1 - e^{-\left(\frac{t}{\alpha}\right)^{\beta}} \quad (1)$$

Here $P_f(t)$ is the probability that a device will fail at a given time, t, i.e. the time when the leakage current has increased by 100x compared to steady-state. α is the reported median time-to-failure (MTTF), i.e. the time where the failure probability is $\frac{1}{e} = 63\ \%$, also known as the Weibull scale. β is the Weibull modulus; the variability in MTTF. The failure times from the reference-set (group E) were fed into the Prokopowicz-Vaskas model to find activation energies, E_A, and voltage acceleration factors at a given temperature, N[20]:

$$\frac{t_1}{t_2} = \left(\frac{V_2}{V_1}\right)^{-N} e^{\frac{E_A}{k_B}\left(\frac{1}{T_1}-\frac{1}{T_2}\right)} \quad (2)$$

t_i, V_i and T_i are the MTTF, voltage, and temperature, respectively, at condition i. k_B is the Boltzmann constant. The lifetime of all stress-tested devices was assessed using moderate acceleration-conditions (T = 175 °C, E = 150 kV/cm). All pristine and stress-tested devices were characterized by optical microscopy.

Figure 2 shows the measured characteristics of each group before and after stress testing. The results are summarized in Table 1. As Figure 2 (a) – (b) indicates, stressing the devices had little to no degrading effects on the investigated electromechanical properties. On the contrary, d_{LS} increased compared to the reference set in all instances apart from after vibration-testing, where the average d_{LS} decreased by 2 %. This general increase is ascribed to device-poling as the initially unpoled devices see unipolar fields during electromechanical characterization. The small-signal angular deflection (5 kV/cm), however, did not change in any of the tests. With regards to the mechanical mirror resonance, softening/stiffening of the nonlinear normal modes with Lissajou-type motion patterns were observed. It is noted that all devices displayed nonlinear Duffing-type resonance[21,22] both before and after stress-testing, as described in more detail in the SI. However, these resonances occur outside the quasi-static to low-frequency (<1 kHz) working regime needed to deflect and stabilize the micromirror's tilt positions.

TVAC, vibration, and unbiased radiation had comparable effects on the polarization and imprint characteristics, as shown in Figure 2 (c) and (d). $2P_R$ decreased in a similar manner as after the initial bipolar cycles of unstressed devices in a lab-scale ambient at room temperature and 35 % relative humidity. This effect was therefore ascribed to normal polarization-stabilization and fatigue-type behavior, as demonstrated for a reference device in the SI. All pristine devices had a small positive self-imprint, i.e., a shift of the hysteresis to larger positive values along the voltage axis. A combination of asymmetric electrodes and the thin film fabrication process is a plausible origin of such imprint. Here the asymmetric electrodes induce an internal field-up of around $\frac{\Phi_{\mathrm{Pt}}-\Phi_{TiW}}{t} = \frac{5.6\ eV-4.4\ eV}{2E-6\ m} = 6.0$ kV/cm. TVAC and vibration-stressed devices developed negative imprints comparable to that of about 5 decades of lab-scale testing at a room-temperature environment, with a rate of 1.4 kV/cm per decade time at 100 kV/cm unipolar field down. According to the interface screening model, imprint arise because of internal dipole alignment with the applied bias, which creates a compensating internal field. In undoped PZT thin films, relatively large concentrations of migrating charged point defects, oxygen vacancies (V_O^{**}) in particular, create defect dipole complexes that align with the applied field. The measured hysteresis imprint is a result of these defect dipole-complexes stabilizing the internal field in one direction. At the same time, charge carriers de-trapping from interfacial layers pins and immobilizes domain wall motion, reducing the polarization and ferroelectric back-switching[23–25]. Figure 3 (a) shows a decreasing $\pm P_R$ and a clockwise rotation of the hysteresis-loop for an unbiased γ-radiated micromirror. Apart from the simultaneous bias and radiation test, this was characteristic for all stressed and unstressed devices, which is in-line with the established models for interface screening and defect-dipole alignment[23–26]. The unbiased γ-radiated devices, however, showed a more pronounced hysteresis-rotation, larger decrease in $2P_R$, and an enhanced imprint compared to TVAC and vibration-stressed devices. This is presumably an effect of the additional photoinduced charges from the high-intensity radiation. Simultaneously biasing the devices during γ-radiation, enhanced the imprint further, and increased $+P_R$. $-P_R$ remained unchanged. This is seen by comparing the pre/post γ-radiation P-E loops in Figure 3 (a) (unbiased) and (b) (biased), and can be explained by the additional photoinduced charges migrating with the applied bias during radiation, thereby changing the polarization-field characteristics[27]. Despite the indication of increased large-signal leakage, Figure 3 (c) and (d) shows that the permittivity and loss were not significantly affected. Zhu et al. have shown that UV radiation can be used as a tool to enhance poling and also enable cold-poling[28,29]. Though γ-radiation and bias are expected to cause similar effects, neither the small-signal deflection nor d_{LS} of the micromirrors increased more than the other stress tests. This suggests that γ-radiation and 50

kV/cm at room temperature is inadequate to markedly enhance device-poling. Despite that the total dose of 1 kGy used here is well below typical literature doses[27,29–32] and well below the radiation hardness of PZT (~50 kGy[31,32]), the results indicate that γ-radiation and bias still induce some radiation-damages even at lower exposure doses.

Figure 4 (a) exemplifies typical leakage vs. time curves for eight inner, eight outer, and eight capacitors, plotted on top of each other in the same graph. The inset images show a representative capacitor before (left) and after (right) failure, with electrothermal breakdown events (ETB) indicated by the red arrows. Generally, the leakage vs. time displayed an initial leakage with a Curie-von Schweidler type behavior ($I(t) \propto t^{-n}$), reaching a stable state for a period before rapidly increasing as the samples electrically degrade[33,34]. The relatively scarce appearance of leakage transients throughout the measurement time for low to moderate acceleration conditions, below 150 kV/cm and 175 °C , correlates well with few or no ETBs on the failed samples. ETB arises as high current densities generate enough heat to locally melt/sublimate the layer-stack materials and can be observed as electrical discharge events[35]. Leakage transients are the archetypical signature of ETB and are regularly encountered for electromechanically degrading piezoelectrics, as well as electrically degrading dielectrics under high bias fields. At higher acceleration temperatures and electrical fields, more leakage transients appeared during electrical degradation, as did the number of post-failure craters (see the SI). This is reasonable as the power dissipation during each ETB increases when the bias increase. Leakage transients in piezoelectric thin films can have several different origins due to their complex electromechanical characteristics[16,17,36]. Post-failure ETBs are often connected by cracks of various extensions, yet the dynamics of their generation before, during, and after ETB is still under discussion[37]. It is noted that both pristine and stressed devices displayed similar leakage-with-time characteristics at 175 °C, and 150 kV/cm, independent of electrode size, electrode location on the die, and die location on the 6" host wafers across multiple fabricated batches. Thus, the material characteristics of the finalized thin-film layer stacks used here appear relatively homogenous, defect-free, and reproducible.

The five groups' failure-probability distribution for the capacitors and inner/outer membrane actuators are shown in Figure 4 (b) and (c), respectively. The Weibull fitting from eq. (1) is summarized in Table 1; the brackets indicate the 95 % confidence interval. The stress-tested devices had MTTF in the range of 1.95-2.64 h, close to 2.11 h as for the reference set. Neither the MTTF nor β showed any clear dependency on the membrane-actuator being the inner or outer ring. TVAC and vibration-stressed devices displayed an increased electrical lifetime, whereas radiation had a decreased electrical lifetime compared to the reference set. This correlates well with the apparent radiation-induced effects on the P-E and C-E loops discussed above. I.e., additional photogenerated carriers contribute to larger leakage and earlier failure. It is noted that, despite being a smaller set, all capacitors had markedly larger MTTF and β-values than the membranes. It is plausible that the capacitors have a smaller distribution of flaws compared to the actuator-membranes due to their considerably smaller surface area and less complex top electrode geometry. The probability distribution of Figure 4 (c) reveals a split into two failure times for the reference and vibration groups, not clearly distinguishable in the other groups. These are split and re-plotted in Figure 4 (d), and contain 7-9 points in each subset. The infant failures are denoted 1 and the secondary failures 2, with corresponding MTTF and Modulus' of $\mathrm{MTTF}_{\mathrm{Ref.1}}$= 0.9 h, $\beta_{\mathrm{Ref.1}}$=13.7, $\mathrm{MTTF}_{\mathrm{Ref.2}}$= 2.6 h, $\beta_{\mathrm{Ref.2}}$=15.0, $\mathrm{MTTF}_{\mathrm{Vib.1}}$= 1.4 h, $\beta_{\mathrm{Vib.1}}$=122.1 and $\mathrm{MTTF}_{\mathrm{Vib.2}}$ = 3.2 h, $\beta_{\mathrm{Vib.2}}$=8.2. The two failure times suggest that devices can experience two failure modes. Considering that the actuator-membranes are allowed to strain considerably more than the capacitors and routings when biased, which theoretically should increase lifetime because of stress-alleviation, it is plausible that the clamped pad and routings are the critical device flaws. ETBs along the routings were generally found to be larger than those along membranes and routings, as illustrated in Figure 4 (e) and (f), possibly due to less mechanical stress-alleviation when electromechanically stressed. The fact that the pads always had a larger MTTF than the actuator-membranes suggests that routings fail before the pads on the reference and vibration

set, similar to observations in previous work in humid conditions[16,17,35]. Yet MTTF increasing for both infant and secondary failures after vibration-testing suggests that failure is more closely related to substrate clamping rather than potential mechanical or thermal damage.

Fitting ln(MTTF) vs. temperature and voltage using eq. (2) resulted in activation energies of $E_{A,O} = 1.030$, $E_{A,I} = 1.032$, $E_{A,P} = 1.091$ for the outer/inner membrane actuators and capacitors, respectively. This is shown in Figure 5 (a) and (b). Presumably, failure is here a result of already established mechanisms related to V_O^{**}-migration and build-up near the cathode region. PZT thin films have a relatively low activation-energy for V_O^{**} migration ($E_A \sim 0.6\ eV$)[38,39]. Also, undoped PZT is inherently acceptor-dominated and has a V_O^{**}-concentration considerably higher than donor-doped PZT, and no multivalent acceptor-dopants, such as Mn to compensate for cathodic charge-injection[40]. Numerous secondary degradation mechanisms induced by cathodic V_O^{**} build-up may lead to electrical failure, and depends on the electrode size and material, film-stoichiometry, polarity of the applied field, and in particular, the thin film processing conditions. Potential mechanisms which correlate with the present activation energies include electron-trapping by Ti^{4+} ($E_A \sim 1.1\ eV$), hole-trapping by lead-vacancies, V_{Pb}'', ($E_A \sim 0.6 - 1.1\ eV$), hole-trapping by acceptor impurities ($E_A \sim 0.6 - 1.3 eV$) or electron-trapping by V_O^{**} ($E_A \sim 1.0 - 1.2\ eV$)[39]. In the absence of visible cracks and ETB (hard breakdown events), it is plausible that devices can be partially rejuvenated from soft breakdown events by reversing the electric field at elevated temperatures and drive V_O^{**} from the cathode interface back into the bulk of the film.

Lastly, voltage acceleration-factors of $N_O = 2.56$, $N_I = 2.59$ and $N_C = 2.88$ V^{-1} were found for the inner/outer actuator-membranes and capacitors, respectively. These are lower than other typically reported values for PZT, typically in the range of 4-5[34,39,41]. Extrapolating the lifetime using eq. (2), the estimated MTTF yields 12 years at 70°C and 1200 years at 30°C at a typical constant operating field of 50 kV/cm.

In conclusion, we have shown that thin film $Pb(Zr,Ti)O_3$-based micromirrors can withstand operating conditions encountered on a space mission without the functional properties degrading. In fact, because of device poling, a general improvement of the functional properties was measured in all instances after stress testing. Moreover, exposure to heavy random and sinusoidal vibrations and thermal cycling in a vacuum considerably increased the median time to failure compared to pristine devices. γ-radiation, on the other hand, caused a larger hysteresis loop imprint and decreased the median time to failure after stressing the devices. The hysteresis inflated, and the lifetime decreased further when the devices were simultaneously irradiated and biased, indicating additional contributions from migrating photoinduced and de-trapped charge carriers. Prokopowich-Vaskas analysis of pristine devices yielded activation energies of 1.03-1.09 eV and voltage acceleration factors of 2.56-2.88 V^{-1}, suggesting failure due to migration and cathodic build-up of oxygen vacancies, extrapolating to a lifetime of 12 years at 70°C. Altogether, the results show that PZT-based thin film MEMS devices are space-ready, and those common stressors encountered in space are expected to be considerably less aggressive than those encountered on Earth, such as humidity.

Supplementary material

See the supplementary material for extended details on test conditions, the effect of stress tests on functional properties and lifetime, leakage with time characteristics for the tested devices, and changes in the resonance characteristics after stress testing.

Acknowledgments

This work was funded by ESA through the project " Short-range high-resolution 3D real-time imaging for robotic vision" (ESA Contract No. 4000129212/19/NL/TFD).

Data availability statement

The data that supports the findings of this study are available within the article and its supplementary material.

References

[1] J. Thorstensen, J.T. Thielemann, P. Risholm, J. Gjessing, R. Dahl-Hansen, and J. Tschudi, Opt. Express **29**, 41081 (2021).

[2] M. Ziemkiewicz, S.R. Davis, S.D. Rommel, D. Gann, B. Luey, J.D. Gamble, and M. Anderson, in *Airborne Intell. Surveillance, Reconnaiss. Syst. Appl. XIII* (2016), p. 982808.

[3] Ø. Skotheim, H. Schumann-Olsen, J. Thorstensen, A.N. Kim, M. Lacolle, K.-H. Haugholt, and T. Bakke, in *Three-Dimensional Image Process. Meas. (3DIPM), Appl. 2015* (International Society for Optics and Photonics, 2015), p. 93930A.

[4] M.K. Mishra, V. Dubey, P.M. Mishra, and I. Khan, J. Eng. Res. Reports **4**, 1 (2019).

[5] C.-B. Eom and S. Trolier-McKinstry, MRS Bull. **37**, 1007 (2012).

[6] S. Trolier-McKinstry, S. Zhang, A.J. Bell, and X. Tan, Annu. Rev. Mater. Res. **48**, 191 (2018).

[7] C.A. Dirdal, P.C. V. Thrane, F.T. Dullo, J. Gjessing, A. Summanwar, and J. Tschudi, Opt. Lett. **47**, 1049 (2022).

[8] M. Chao, T. Paul C. V., D. Fei, G. Jo, T. Martin, W. Cuo Wu, D. Christopher, and B. Sergey I., Sci. Adv. **7**, (2021).

[9] G. Esteves, C.M. Fancher, M. Wallace, R. Johnson-Wilke, R.H.T. Wilke, S. Trolier-McKinstry, R.G. Polcawich, and J.L. Jones, Mater. Des. **111**, 429 (2016).

[10] M.T. Todaro, F. Guido, V. Mastronardi, D. Desmaele, G. Epifani, L. Algieri, and M. De Vittorio, Microelectron. Eng. (2017).

[11] Y. Qiu, J. V Gigliotti, M. Wallace, F. Griggio, C.E.M. Demore, S. Cochran, and S. Trolier-McKinstry, Sensors (Switzerland) **15**, 8020 (2015).

[12] Y. Kusano, Q. Wang, G.L. Luo, Y. Lu, R.Q. Rudy, R.G. Polcawich, and D.A. Horsley, J. Microelectromechanical Syst. **27**, 296 (2018).

[13] H.S. Choi, J.L. Ding, A. Bandyopadhyay, M.J. Anderson, and S. Bose, J. Micromechanics Microengineering **18**, 025037 (2008).

[14] T. Bakke, A. Vogl, O. Zero, F. Tyholdt, I.R. Johansen, and D. Wang, J. Micromechanics Microengineering **20**, 1 (2010).

[15] V. Cotroneo, W.N. Davis, P.B. Reid, D.A. Schwartz, S. Trolier-McKinstry, and R.H.T. Wilke, in *Opt. EUV, X-Ray, Gamma-Ray Astron. V*, edited by S.L. O'Dell and G. Pareschi (International Society for Optics and Photonics, 2011), p. 81471R.

[16] R.P. Dahl-hansen, F. Tyholdt, J. Gjessing, A. Vogl, P. Wittendorp, J. Vedum, and T. Tybell, 1 (2020).

[17] R.P. Dahl-Hansen, J.M. Polfus, E. Vøllestad, B. Akkopru-Akgun, L. Denis, K. Coleman, F. Tyholdt, S. Trolier-Mckinstry, and T. Tybell, J. Appl. Phys. **127**, 244101 (2020).

[18] J.B. Quinn and G.D. Quinn, Dent. Mater. **26**, 135 (2010).

[19] W. Zhu, B. Akkopru-Akgun, and S. Trolier-McKinstry, Appl. Phys. Lett. **111**, 212903 (2017).

[20] W.J. Minford, IEEE Trans. Components, Hybrids, Manuf. Technol. **5**, 297 (1982).

[21] H.-P. Yeh, Y.-C. Chien, and J.-Y. Tu, in *ASME 2016 Conf. Inf. Storage Process. Syst.* (ASME, 2016), p. V001T07A013.

[22] R. Lifshitz and M.C. Cross, in *Rev. Nonlinear Dyn. Complex.* (2009), pp. 1–52.

[23] M. Grossmann, O. Lohse, D. Bolten, U. Boettger, and R. Waser, J. Appl. Phys. **92**, 2688 (2002).

[24] B. Akkopru-Akgun, W. Zhu, M.T. Lanagan, and S. Trolier-McKinstry, J. Am. Ceram. Soc. 1 (2019).

[25] M. Grossmann, O. Lohse, T. Schneller, D. Bolten, U. Boettger, J.R. Contreras, H. Kohlstedt, and R. Waser, in *Integr. Ferroelectr.* (2001), pp. 205–214.

[26] M. Grossmann, O. Lohse, D. Bolten, U. Boettger, T. Schneller, and R. Waser, J. Appl. Phys. **92**, 2680 (2002).

[27] S.A. Yang, B.H. Kim, M.K. Lee, G.J. Lee, N.H. Lee, and S.D. Bu, Thin Solid Films **562**, 185 (2014).

[28] W. Zhu, W. Luo, B. Akkopru-Akgun, M. Lanagan, C.A. Randall, and S. Trolier-McKinstry, J. Mater. Sci. **53**, 7180 (2018).

[29] R.Q. Rudy, K.M. Grove, M. Rivas, J. Guerrier, C. Cress, R.R. Benoit, J.L. Jones, E. Glaser, S. Brewer, N. Bassiri-Gharb, and R.G. Polcawich, IEEE Trans. Ultrason. Ferroelectr. Freq. Control **64**, 1135 (2017).

[30] S.C. Lee, R.D. Schrimpf, K.F. Galloway, G. Teowee, D.P. Birnie, and D.R. Uhlmann, IEEE Trans. Nucl. Sci. **39**, 2036 (1992).

[31] J.M. Benedetto, R.A. Moore, F.B. McLean, P.S. Brody, and S.K. Dey, IEEE Trans. Nucl. Sci. **37**, 1713 (1990).

[32] J.F. Scott, C.A. Araujo, H.B. Meadows, L.D. McMillan, and A. Shawabkeh, J. Appl. Phys. **66**, 1444 (1989).

[33] H.N. Al-Shareef and D. Dimos, J. Am. Ceram. Soc. **80**, 3127 (2005).

[34] D. Monteiro Diniz Reis, S. Rzepka, and K. Hiller, Microelectron. Reliab. **88**–**90**, 835 (2018).

[35] R.P. Dahl-Hansen, T. Tybell, and F. Tyholdt, in *2018 IEEE ISAF-FMA-AMF-AMEC-PFM Jt. Conf. IFAAP 2018* (IEEE, 2018), pp. 1–4.

[36] W. Zhu, T. Borman, K. DeCesaris, B. Truong, M.M. Lieu, S.W. Ko, P. Mardilovich, and S. Trolier-McKinstry, J. Am. Ceram. Soc. **102**, 1734 (2018).

[37] K. Coleman, J. Walker, W. Zhu, S.W. Ko, P. Mardilovich, and S. Trolier-Mckinstry, in *IFCS-ISAF 2020 - Jt. Conf. IEEE Int. Freq. Control Symp. IEEE Int. Symp. Appl. Ferroelectr. Proc.* (Institute of Electrical and Electronics Engineers Inc., 2020).

[38] D. Damjanovic, Rep. Prog. Phys **61**, 1267 (1998).

[39] B. Akkopru-Akgun, T.J.M. Bayer, K. Tsuji, C.A. Randall, M.T. Lanagan, and S. Trolier-McKinstry, Acta Mater. **208**, 116680 (2021).

[40] W. Zhu, B. Akkopru-Akgun, J.I. Yang, C. Fragkiadakis, K. Wang, S.W. Ko, P. Mardilovich, and S. Trolier-McKinstry, Acta Mater. **219**, 117251 (2021).

[41] S.W. Ko, W. Zhu, C. Fragkiadakis, T. Borman, K. Wang, P. Mardilovich, and S. Trolier-McKinstry, J. Am. Ceram. Soc. **102**, 1211 (2019).

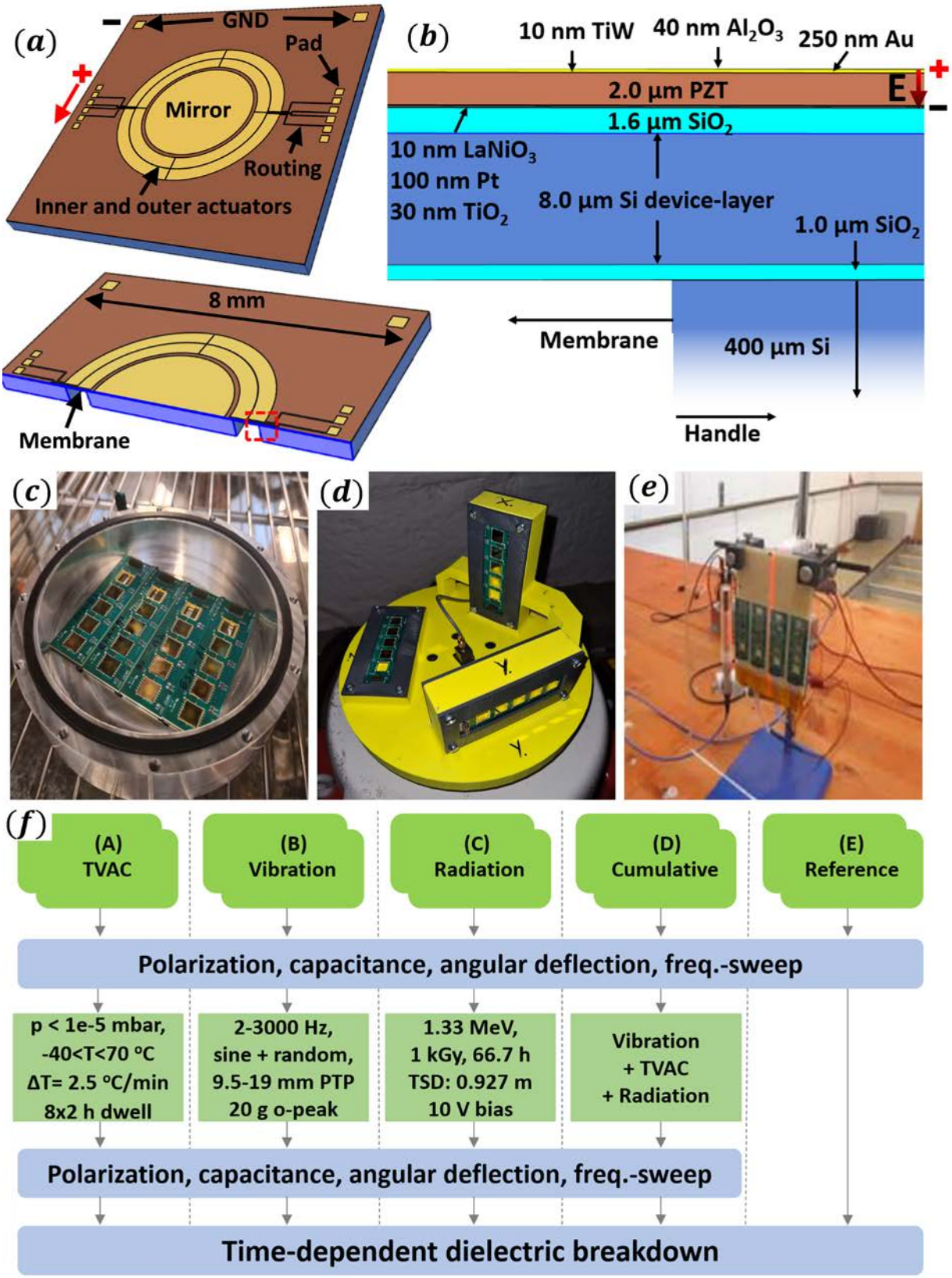

Figure 1. (a) and (b) schematically show the finalized micromirror structure and the functional layer to scale. (a) shows the device constituents and a section-cut and (b) a cross-section of the layer-stack and polarity. Micromirrors mounted for TVAC, vibration, and γ-radiation stress test (c)-(e); and schematic representation of the test sequence (f).

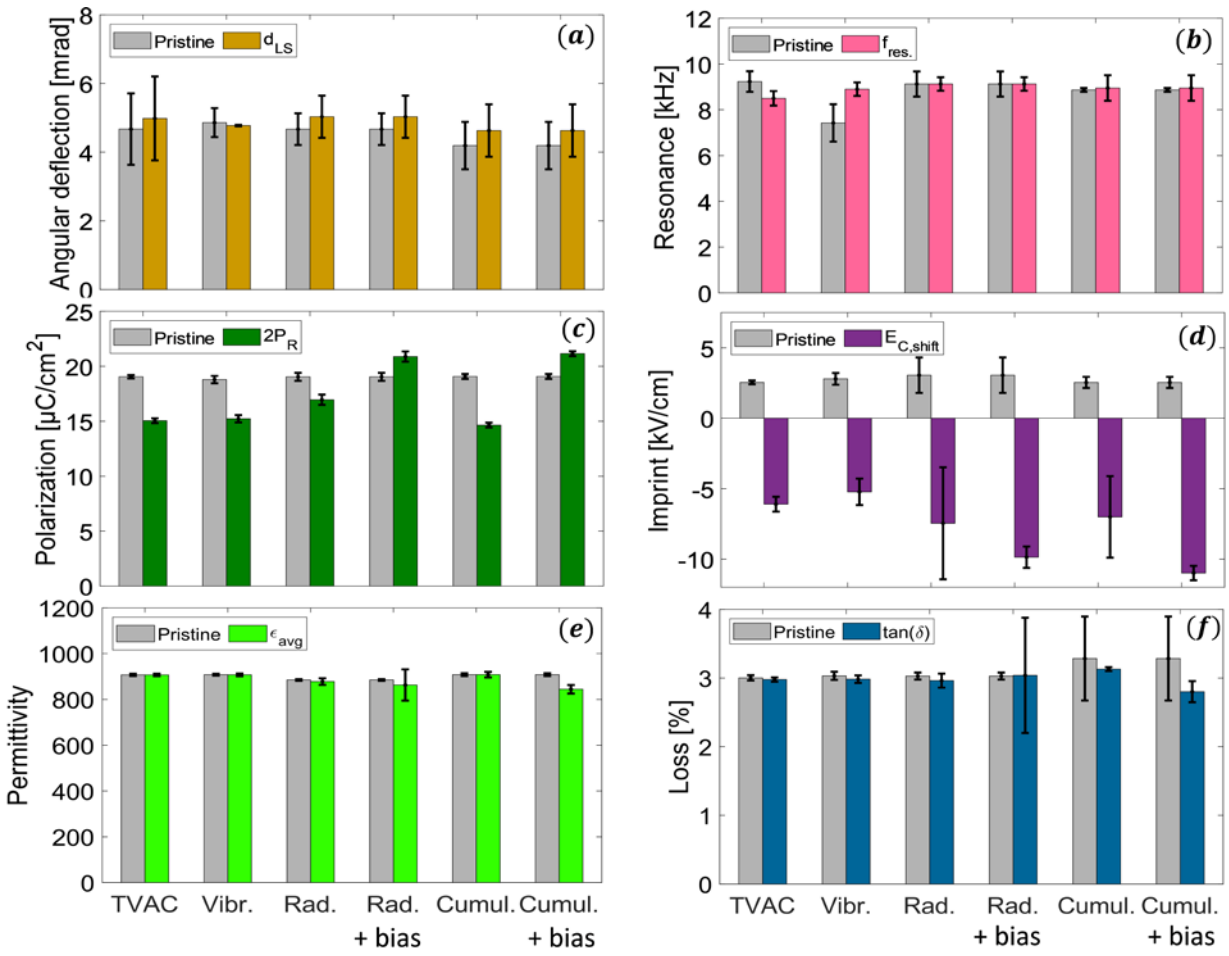

Figure 2: (a); large-signal angular deflection (d_{LS}), (b); small-signal resonance frequency (f_{res}), (c); remnant polarization ($2P_R$), (d); imprint, ($E_{C,shift}$), (e); average permittivity (ε_{avg}) and (f); loss tangent ($tan(\delta)$) after stress-testing. The light grey bars show pristine values. The black error bars show the standard deviations for each set.

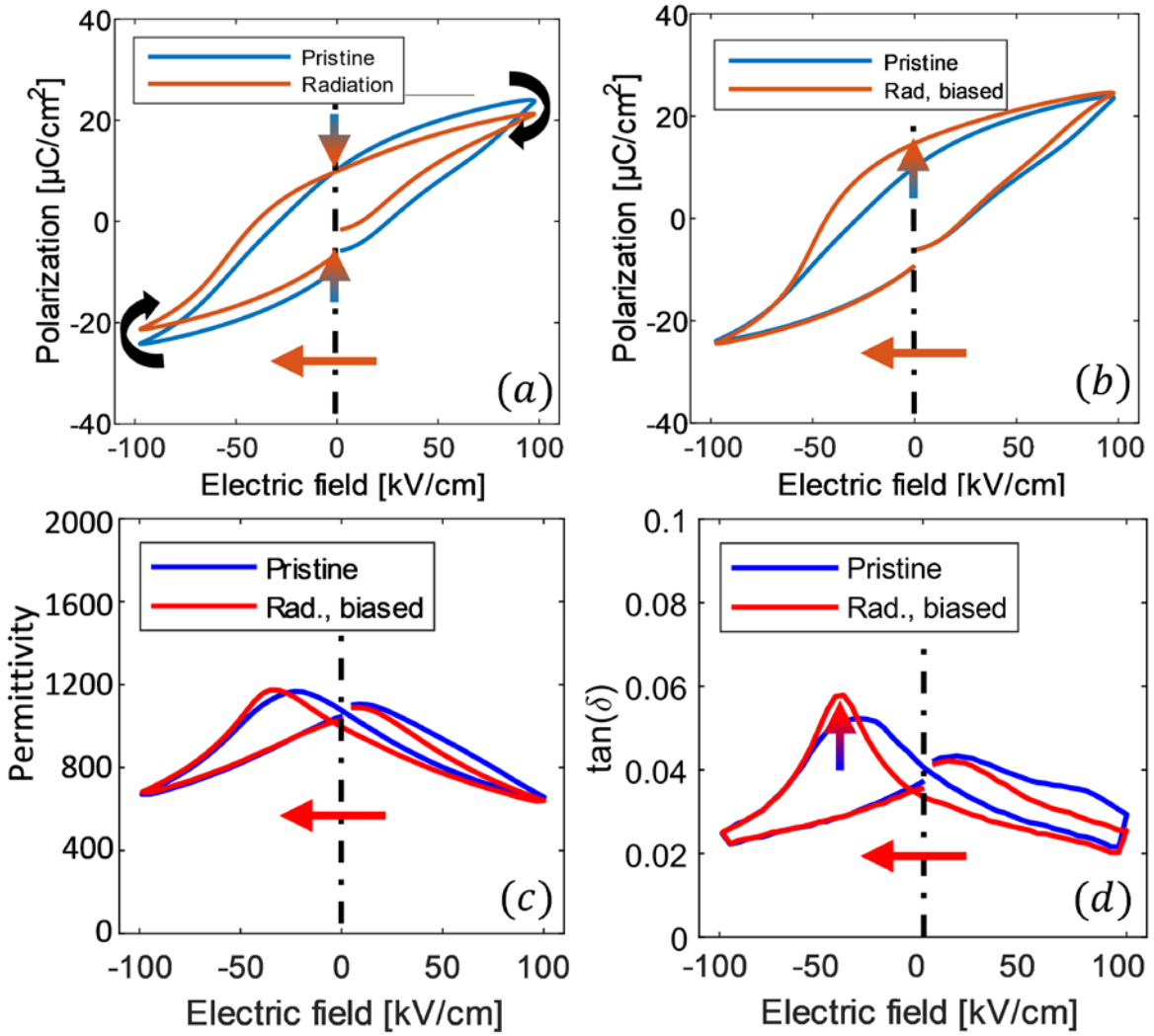

Figure 3: General trends in ferroelectric hysteresis upon γ-radiation without (a) and with (b) applied bias. Permittivity and loss after simultaneous radiation and bias are shown in (c) and (d), respectively.

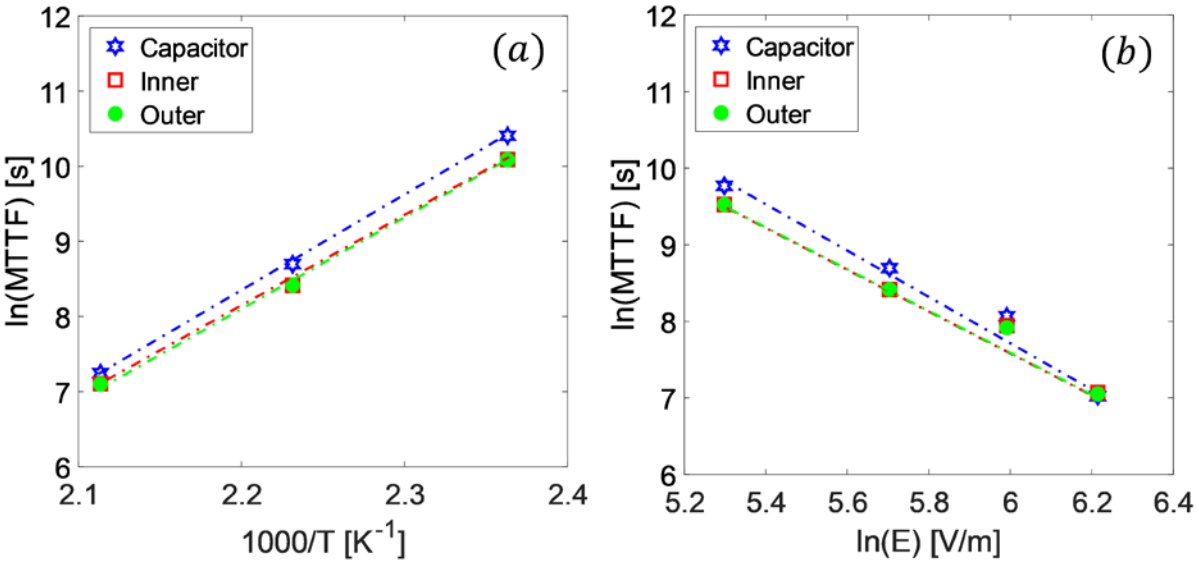

Figure 5: Fitting and calculation of activation-energy, (a), and voltage acceleration-factor, (b).

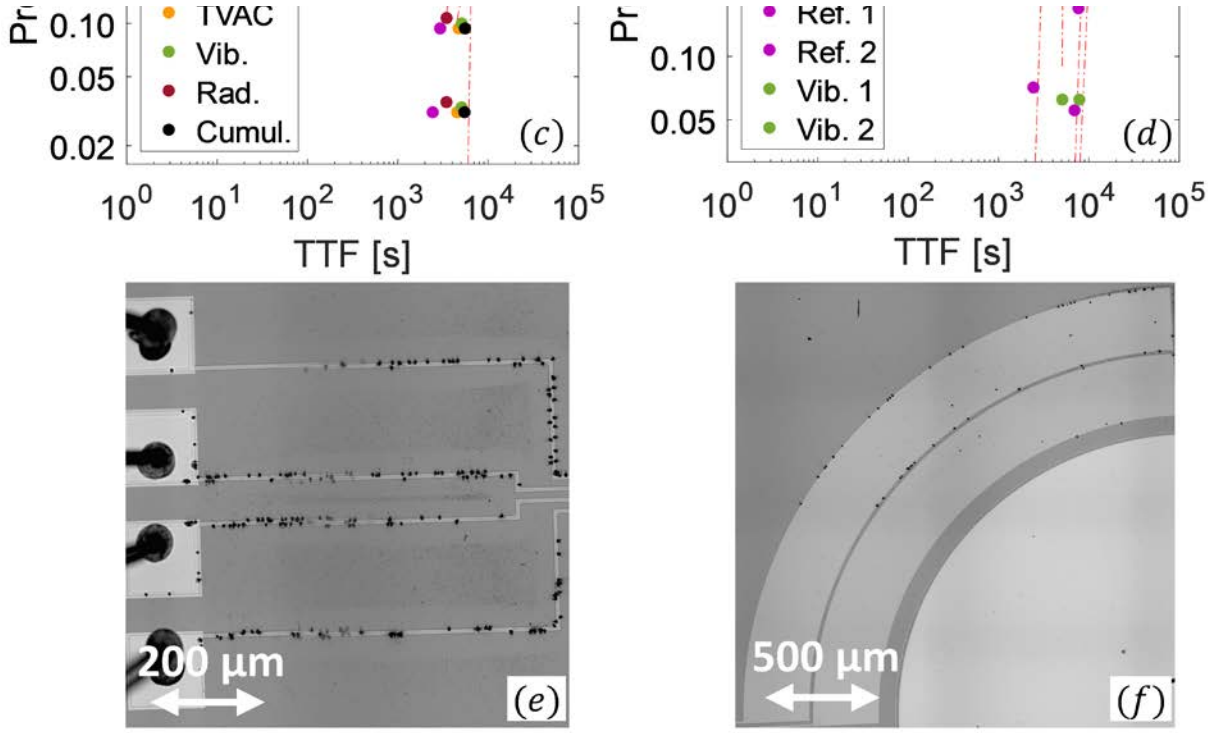

Figure 4: Typical TDDB measurement (175 °C, 150 kV/cm) illustrated for a TVAC-tested set of devices; eight capacitors, eight inner and eight outer membrane sections, (a). The inset image shows a micrograph of typical failure sights before and after TDDB. The absence of transient currents is noticeable. (b) and (c) show failure probability distributions exemplified for the five groups for capacitors, (b), and membranes, (c), respectively. (d) shows the splitting of failure times for the reference and vibration-tests with 7/9 samples in Ref.1/Ref2 and 8/8 samples in Vib.1/Vib.2. Electrothermal breakdown events were observed along pads and routings, (e), as well as on membranes, (f).

Table 1: Measured overall pristine, post-test, and cumulative averages for the various stress tests.

Test	d_{LS} [mrad]	$f_{res,SS}$ [kHz]	$2P_R \left[\frac{\mu C}{cm^2}\right]$	$E_C^+ \left[\frac{kV}{cm}\right]$	$E_{C,shift} \left[\frac{kV}{cm}\right]$	ε_{avg}	$\tan(\delta)$ [%]	MTTF x10^3 [s], β [95%], I/O	MTTF x10^3 [s], β [95%], cap.
Pristine (avg. all)	4.5 ± 0.6	8.5 ± 0.8	19.0 ± 0.1	30.9 ± 0.3	2.6 ± 0.3	908 ± 5	3.1 ± 0.1	7.6, 3.1 [6.6 – 8.7]	7.9, 7.7 [7.2 – 8.7]
TVAC	5.0 ± 1.2	8.5 ± 0.3	15.0 ± 0.1	21.4 ± 0.8	-6.1 ± 0.5	907 ± 5	3.0 ± 0.3	9.0, 4.0 [7.9 – 10.3]	10.4, 6.2 [9.2 – 11.7]
Vibration	4.8 ± 0.1	8.9 ± 0.3	15.2 ± 0.1	22.3 ± 1.1	-5.2 ± 0.9	907 ± 6	3.0 ± 0.3	8.8, 2.8 [7.3 – 10.6]	10.7, 2.4 [7.5 – 15.4]
Radiation no bias	5.0 ± 0.6	9.1 ± 0.3	16.9 ± 0.3	21.0 ± 2.2	-7.5 ± 4.0	878 ± 10	2.9 ± 0.1	7.0, 9.5 [6.7 – 7.4]	8.2, 8.6 [7.5 – 8.9]
Radiation 10 V bias	5.0 ± 0.6	9.1 ± 0.3	20.9 ± 1.6	22.7 ± 2.1	-9.9 ± 0.8	863 ± 68	3.9 ± 0.8	7.0, 4.4 [6.4 – 7.8]	7.5, 7.4 [7.1 – 7.9]
Cumulative no bias	4.6 ± 0.7	8.6 ± 0.3	14.6 ± 0.9	34.6 ± 2.1	-7.0 ± 3.6	908 ± 12	3.1 ± 0.1	7.4, 9.8 [6.8 – 7.9]	7.5, 6.6 [6.6 – 8.5]
Cumulative 10 V bias	4.6 ± 0.7	8.6 ± 0.3	21.1 ± 2.0	22.2 ± 2.2	-11.0 ± 0.5	844 ± 18	2.8 ± 0.2	7.0, 4.6 [5.9 – 8.3]	7.4, 2.5 [5.5 – 9.9]